ESTIMATION OF SPEED OF SOUND IN DUAL-LAYERED MEDIA USING MEDICAL ULTRASOUND IMAGE DECONVOLUTION

H.-C. Shin, R. W. Prager,
W. H. Gomersall, N. G. Kingsbury,
G. M. Treece and A. H. Gee

CUED / F-INFENG / TR 637

15 September 2009

Department of Engineering
University of Cambridge
Trumpington Street
Cambridge, CB2 1PZ
United Kingdom

Email:
hs338/rwp/whg21/ngk/gmt11/ahg@eng.cam.ac.uk

Estimation of Speed of Sound in Dual-Layered Media using Medical Ultrasound Image Deconvolution

Ho-Chul Shin, Richard Prager, Henry Gomersall,
Nick Kingsbury, Graham Treece and Andrew Gee

Department of Engineering, University of Cambridge,
Trumpington Street, Cambridge, CB2 1PZ, United Kingdom

Abstract

The speed of sound in soft tissues is usually assumed to be 1540 m/s in medical pulse-echo ultrasound imaging systems. When the true speed is different, the mismatch can lead to distortions in the acquired images, and so reduce their clinical value. Previously we reported a new method of sound-speed estimation in the context of image deconvolution. Unlike most other sound-speed estimation methods, this enables the use of unmodified ultrasound machines and a normal scanning pattern. Our approach was validated for largely homogeneous media with single sound speeds. In this article, we demonstrate that sound speeds of dual-layered media can also be estimated through image deconvolution. An ultrasound simulator has been developed for layered media assuming that, for moderate speed differences, the reflection at the interface may be neglected. We have applied our dual-layer algorithm to simulations and *in vitro* phantoms. The speed of the top layer is estimated by our aforesaid method for homogeneous media. Then, when the layer boundary position is known, a series of deconvolutions are carried out with dual-layered point-spread functions having different lower-layer speeds. The best restoration is selected using a correlation metric. The error level for *in vitro* phantoms is found to be not as good as that of our single-speed algorithm, but is comparable to other local speed estimation methods where the data acquisition may not be as simple as in our proposed method.

Keywords: Medical ultrasound image; Dual-layered media; Non-blind deconvolution; Point-spread function; Speed of sound; Sound estimation.

1 Introduction

Pulse-echo medical ultrasound imaging usually assumes the speed of sound is 1540 m/s in soft tissue for the beamforming delay profile and the display of acquired images. The current convention of using the assumed speed leads to distortions in B-mode images when the actual speed of sound is different. The effects of errors in the sound speed, such as degraded spatial resolution, have been

widely reported, and some of the consequences have been quantified [1]. Therefore, the estimation of the correct acoustic speed is beneficial in improving the overall image quality and hence in increasing its diagnostic value. At the same time, the estimated speed of sound itself has its own significance in the context of tissue characterisation.

The speed of medical ultrasound has been estimated using transmission methods, which measure the time taken while a pulse propagated between a transmitter and a receiver. But clinical applications were limited to the breast [2]. Robinson et al. [3] carried out an extensive review of pulse-echo sound-speed estimation techniques. Nine methods in three categories were examined in detail. Most of the reviewed methods produce the average speed of sound in the scanned tissues. Only a few were capable of local speed estimation. Kondo et al. [4] reported the estimation of *in vivo* local speed of sound by using a few pairs of crystal elements in a linear array. But, they stated that an exact measurement of local sound speed was difficult. Ophir and Yazdi [5] applied a transaxial compression technique to a dual-layered *in vitro* phantom. The technique involves a precise movement of a transducer which compresses the phantom surface. The acquisition of multiple scans after compression can be carried out by a single transducer, but this is often accompanied by a second transducer to compensate for potential movement of the region of interest caused by compression of the phantom surface.

Recently, a detailed local sound-speed estimation of biological tissue was demonstrated using ultrasound based on a scanning acoustic microscope (SAM) [6] and computed tomography (CT) [7, 8, 9, 10, 11]. However, the signal carrier frequency of SAM system reaches as high as 500 MHz, and as in other microscope techniques non-invasive measurement is not possible. The CT systems have been demonstrated in a recent pre-clinical trial [11] to be capable of the detailed estimation of sound speed as well as attenuation. However, its use of transmission ultrasound is limited to breast imaging. It is also different from the pulse-echo approach addressed in this paper and requires higher system complexity like other CT systems.

Our research group has recently published a novel speed-of-sound estimation technique by using image deconvolution [12]. The algorithm is based on the assumption that soft tissue is macroscopically homogeneous and its underlying speed of sound is constant. Our published technique has several advantages over other methods of medical ultrasound speed estimation [3]. The data can be collected by a single scan using a single transducer array unlike other methods [2, 3, 13]. No transducer movement is required, whereas precise movement is a commonplace requirement in other techniques [3, 5]. No special rigs are necessary in holding the transducer to satisfy a geometric constraint inherent as in some other methods [3, 14]. In other words, conventional use of a transducer array is sufficient for our algorithm.

The fundamental concept enabling the speed estimation in our method is image deconvolution [15, 16, 17]. The advantage of using non-blind deconvolution is that we do not need multiple ultrasound scans, as some other methods do in order to adjust their beamforming time delays [2, 13]. Necessary variations can be easily accomplished off-line by adjusting the point-spread function (PSF) in our deconvolution framework.

However, our original approach was not capable of handling inhomogeneous tissues. As an idealised scenario of non-uniform soft tissue, we now consider a layered medium formed of two layers with different sound speeds. We demonstrate that image deconvolution can be used to estimate sound speed in such an environment.

The rest of the paper is arranged into the following sections: Section 2 describes the modelling of ultrasound behaviour in dual-layered media, and explains the development of an ultrasound simulator applicable to layered media. Section 3 presents the results of the simulations together with the method of estimating the speed. Section 4 addresses the speed estimation of *in vitro* phantoms. Finally, conclusions are drawn and it is followed by a brief introduction to our non-blind deconvolution algorithm in the appendix.

2 Medical ultrasound in dual-layered soft tissue

An acoustic wave, of which an ultrasound wave may be considered a subset, is reflected and transmitted when it encounters the boundary between different media. In general, the phenomenon of transmission is complicated. However, the situation can be eased when the acoustic wave front and the medium boundary are planar and the involved media are all considered to be fluids rather than solids (see p.124 in [18]).

Here, we define a fluid to be a medium where propagation of a longitudinal wave is dominant, whereas a solid is a medium in which longitudinal and transverse waves are free to propagate. In fluids the path of a refracted wave is easily determined by the refractive index, but solids are often anisotropic and hence the direction of a transmitted wave is influenced by local structure.

In soft tissue, transverse waves have a low propagation speed of around 100 m/s. They are severely attenuated at frequencies over 1 MHz and can therefore be neglected at diagnostic powers (see p.1.4 in [19]). Also in their composition, soft tissues are mainly made of water with a few solid components added. Therefore, in diagnostic medical ultrasound imaging, soft tissues can usually be approximated as a fluid.

2.1 Reflection in dual-layered soft tissues

It is widely known that most normally-incident ultrasound energy is transmitted at the boundary between different types of soft tissues. A very small fraction of the energy is reflected, of which the strongest (power reflection coefficient, $\mathbf{R} \approx 0.01$) occurs along muscle-fat interface (see p.1.19 and Table 1-8 in [19]). But for ultrasound probes consisting of arrays of piezoelectric elements, oblique incidence does occur regardless of transducer positioning. For oblique incidence, the coefficient $\mathbf{R}$ at the fluid-fluid boundary is given by (see p.132 [18]):

$$\mathbf{R} \;=\; \left| \frac{(\rho_2/\rho_1)\; c_2/c_1 \;-\; \cos\theta_2/\cos\theta_1}{(\rho_2/\rho_1)\; c_2/c_1 \;+\; \cos\theta_2/\cos\theta_1} \right|^2 . \tag{1}$$

Here, the symbols ρ, c and θ indicate density, sound speed and angle of wave propagation, respectively. The subscripts 1 and 2 denote the layers 1 of the incident and 2 of the refracted. Symbols c_1, c_2, θ_1 and θ_2 are related according to Snell's law (see Eq. (2) and Fig. 2). Equation (1) is valid when the refracted angle θ_2 is real, otherwise the coefficient $\mathbf{R}$ is unity. The angle θ_2 becomes complex when the incident angle θ_1 is bigger than a critical angle determined by the ratio of both speeds of sound.

Examples of the coefficient $\mathbf{R}$ relevant to one of our ultrasound probes are shown in Fig. 1. The ultrasound probe has 32 active piezoelectric elements whose geometric centres are laterally spread from -3.0535 to $+3.0535$ mm with an interval of 0.197 mm. Speed differences, $c_2 - c_1$, were

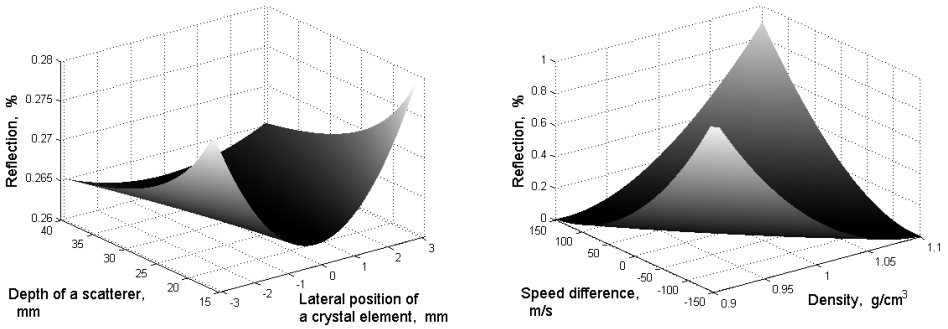

Figure 1: Power reflection coefficient $\mathbf{R}$ at a boundary depth of 16 mm. Subplot (a) shows $\mathbf{R}$ as a function of scatterer depth and of crystal element position, for a speed difference of -150 m/s with a layer-2 density of 1 g/cm^3. Subplot (b) shows $\mathbf{R}$ as a function of the speed difference between layers and of layer-2 density, for a crystal element located at -3.0535 mm and a scatterer depth of 25 mm. Note the coefficient is displayed as a percentage and the z-axis range is different in (a) and (b).

investigated in the range from -150 to $+150$ m/s when $c_1 = 1540$ m/s. The sound speed of most biological materials except bone falls well within the range: the lower end of fat being 1440 m/s; the higher end of muscle at 1626 m/s (see Table 1-1 in [19]). Note that quoted values are slightly different depending on the source of information. The density of layer 1 was chosen as 1 g/cm^3, which is equivalent to that of water. The density of layer 2 was varied from 0.9 to 1.1 g/cm^3, which covers most forms of soft tissues: from 0.95 g/cm^3 for fat to 1.07 g/cm^3 for muscle (see Table 1-1 in [19]). The depth of a scatterer in layer 2 is varied from 16.1 to 40.0 mm when the boundary is located at a depth of 16 mm.

These graphs show that the coefficient $\mathbf{R}$ is mostly affected by differences in speed and density, and also imply that the extra effect of oblique incidence is not significant. In general the amount of the reflection is very low. Only the extreme combinations of sound speed and density see the reflection reach 1 % of the incident energy. We are therefore reassured that most of ultrasound energy is transmitted and hence the reflection can be ignored.

This assumption of the reflection being ignored not only simplifies the ultrasound image formation for the bottom layer but also validates the use of deconvolution in the top layer. Our deconvolution algorithm like many other linear deconvolution models assumes the first-order Born approximation, which results in the sonification of scatterers by waves directly from transducer elements. Therefore, strong reflections at the boundary could generate secondary sources which would reduce the accuracy of our deconvolution in the top-layer part of the media.

2.2 Refraction in dual-layered media

In creating PSFs with dual-layer characteristics, the determination of the path intersection with the boundary is of paramount importance. Its location will decide the difference between the refracted path of the ultrasound and the straight path as if there were only a single homogeneous layer between the scatterer and the piezoelectric element. This difference in distance and subsequently in arrival time will generate an overall perception of B-mode image distortion when soft tissue is composed of layers with different speeds of sound.

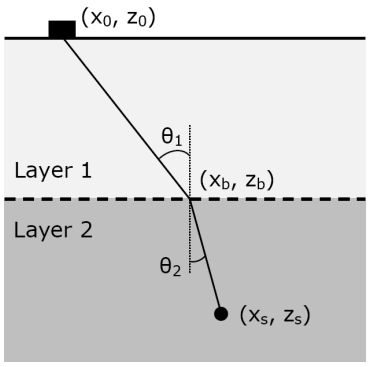

Figure 2: Schematic diagram showing the geometric relationship between incident and refracted ultrasound waves in a fluid. The position of the transmit or receive crystal element is denoted by (x_0, z_0), that of the scatterer by (x_s, z_s), and that of the path intersection with the boundary by (x_b, z_b). All three of these points are assumed to be in a plane and to have the same y-coordinate.

When both media at the boundary are isotropic such as fluid, the well-known Snell's law may be applied to establish the relationship between the speeds in the adjacent media and the angles of incidence and refraction of plane waves (see p.131 in [18]):

$$\frac{\sin\theta_1}{c_1} = \frac{\sin\theta_2}{c_2} \,. \tag{2}$$

The geometric relationship is shown in Fig. 2. Each layer is assumed to be macroscopically homogeneous and isotropic, and hence to have uniform macroscopic properties. But the media may be considered microscopically inhomogeneous enough to have back scattering from the ultrasound wave. The position of the transmit or receive crystal element is denoted by (x_0, z_0), that of the scatterer by (x_s, z_s), and that of the interaction point at the boundary by (x_b, z_b). All three pairs of points are assumed to be in a plane and to have the same y-coordinate. This constraint can be easily met by a coordinate transformation. The medium boundary is assumed to be semi-infinite and parallel to the transducer aperture. Since our deconvolution algorithm like others assumes shift invariance in the lateral dimension of the probe, the medium boundary and the probe surface are required to be parallel to each other. Layer 1 has a uniform sound speed of c_1 and layer 2 has c_2. The incidence and refraction angles on the boundary are denoted by θ_1 and θ_2, respectively. Hence, the squared version of Eq. (2) becomes:

$$\frac{1}{c_1^2}\frac{(x_b - x_0)^2}{(z_b - z_0)^2 + (x_b - x_0)^2} = \frac{1}{c_2^2}\frac{(x_s - x_b)^2}{(z_s - z_b)^2 + (x_s - x_b)^2} \,. \tag{3}$$

In our problem formulation, all variables in Eq. (3) apart from the lateral location on the boundary (x_b) are assumed to be known including the depth of the boundary (z_b). A few steps of simple arithmetic from Eq. (3) leads to the following quartic equation:

$$p_4\, x_b^4 + p_3\, x_b^3 + p_2\, x_b^2 + p_1\, x_b + p_0 = 0 \,, \tag{4}$$

where coefficients are arranged as follows, when the crystal element is placed at the origin of the coordinate system $(x_0 = 0,\ z_0 = 0)$:

$$p_4 = 1 - \delta^2 \; ; \qquad \delta = \; c_1 \,/\, c_2 \; ;$$

$$p_3 = -2\, x_s\, p_4 \; ;$$

$$p_2 = (z_s - z_b)^2 + x_s^2 - \delta^2 (z_b^2 + x_s^2) \; ;$$

$$p_1 = 2\, x_s\, z_b^2\, \delta^2 \; ; \qquad p_0 = -\, \delta^2\, z_b^2\, x_s^2 \; .$$

The quartic equation can be solved numerically for example via the Matlab command *roots.m*, and leads to a single unique solution of x_b through the constraint of it being real and positioned between the transducer element and the scatterer in question. Once x_b is determined, the calculation of the refracted arrival time is straightforward. The concept for the dual-layer situation can be easily extended to media with more than two layers, but the solution will involve a system of quartic equations.

Strictly, the relations in Eqs. (2) to (4) are valid for a single frequency. For dispersive media, these need to be evaluated for all frequencies of interest. However, for soft tissue, the degree of dispersion is so low that it can be neglected (see p.4.5 in [19]). Hence, a single calculation is sufficient.

2.3 Dual-layer ultrasound simulator

We have built an in-house ultrasound simulator for dual-layered media. The code is composed mainly of two steps: first, calculation of pressure fields in dual-layered media from individual piezo-electric elements and second, beamforming of these elemental responses. The first step is based on an approach applied to homogeneous media by Jensen and Svendsen [20]. They simulated pulsed pressure fields from arbitrarily shaped ultrasound transducers. A physical crystal element was mathematically divided into small rectangles, and a "spatial impulse response" (SIR) was calculated for each rectangle and summed over the physical element. A far-field approximation was also used to speed up the calculation.

The main difference between the Jensen-Svendsen simulator and our dual-layer implementation lies in formation of the SIR for the bottom layer. Figure 3 illustrates the situation, which is an idealised case of two-dimensional interaction for brevity. Diagram (a) corresponds to an homogeneous medium studied by Jensen and Svendsen and diagram (b) shows the refraction pattern in the dual-layer case. The "sub-crystal" label in the diagram indicates that each individual crystal element is divided into a collection of smaller areas. The sub-crystal elements must be small enough to make the far-field approximation valid [20].

The effects of these t_c, t_1 and t_2 are collectively known as the SIR. The arrival time t_c indicates how far the scatterer is located away from the sub-crystal element. The difference $|t_2 - t_1|$ determines the shape of the SIR and eventually the shape of the waveform received or transmitted by the physical element composed of sub-crystals. When a far-field approximation is valid, the arrival times t_1 and t_2 are symmetrically separated from the central time t_c in homogeneous media, but they are not in inhomogeneous media. Therefore, the refracted arrival times t_1 and t_2 should be evaluated individually for the bottom layer of dual-layered media using Eq. (4) where (x_0, z_0) now corresponds to edges of sub-crystals. It is also noted that, for the top layer of dual-layered media, our ultrasound simulator follows the same approach taken by Jensen and Svendsen.

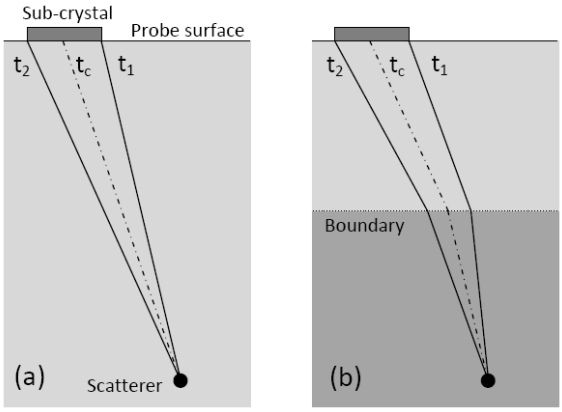

Figure 3: Schematic diagram showing spatial response of a transducer element and a scatterer. Diagram (a) is what happens in homogeneous media. Diagram (b) is what may happen in dual-layer media. Symbols t_c, t_1 and t_2 indicate the arrival times along the paths.

Once a SIR for a given scatterer and a given physical element is determined after summation of SIRs in sub-crystals, the corresponding pressure field at the scatterer position is determined by convolution of the SIR and the electro-mechanical impulse response of the element. For pulse-echo response, convolution is conducted twice for a pair of transmit and receive elements. Then, the final part of beamforming to focus the ultrasound is straightforward. This dual-layer ultrasound simulator has been used to calculate PSFs throughout this article.

3 Method and Simulations

We applied our sound-speed estimation technique to dual-layered two-dimensional simulated phantoms. The way the simulation was conducted is explained in this section. We start with examples illustrating how ultrasound images may behave when there is a layered change in the speed of sound.

3.1 Simulated reflectivity function

A two-dimensional simulated phantom was created with five circles whose geometry is shown in Fig. 4. This five-circle configuration has macroscopically piecewise-smooth features. The bright circles are ten times stronger than the background, the dark ones are ten times weaker, and the medium one is three times stronger. The reflectivity of each scatterer is then randomised by incorporating a Gaussian distribution which represents microscopic fluctuations. A reference image for the reflectivity function is displayed in Fig. 4a.

3.2 Simulated ultrasound image formation

We blur the reflectivity function by calculating a forward convolution of the image in Fig. 4a with the PSF evaluated to have a dual-layered characteristic. The convolution algorithm itself is essentially the same as that used in the single-layered medium [12, 17].

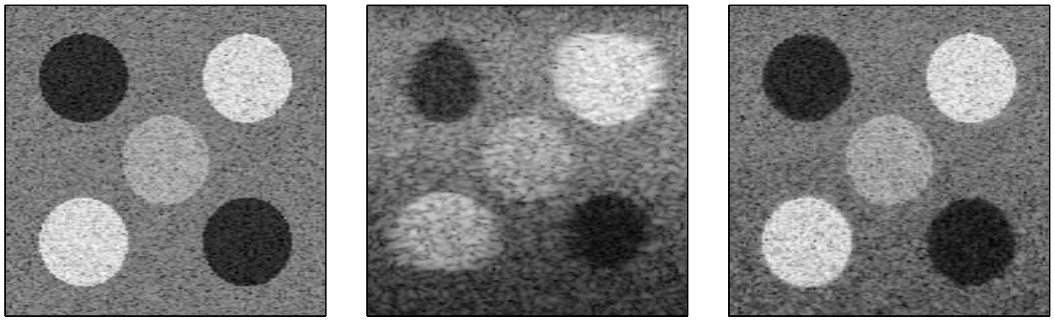

Figure 4: Behaviour of a dual-speed layered medium with the layer boundary at the centre of the middle circle. (a) the simulated reflectivity function, (b) the simulated ultrasound image in which the speed of the top layer is 1540 m/s and that of the bottom layer is 250 m/s faster, and (c) the deconvolved image. B-mode images were constructed assuming the sound speed of 1540 m/s. The dynamic range of the logarithmically compressed images is 60 dB.

This dual-layered PSF is designed to have the layer boundary at the centre of the middle circle. The speed of the top layer in the image (b) is 1540 m/s. The speed of the bottom layer is 1790 m/s. An excessive difference in speed was chosen to produce a clear demonstration of the dual-layer behaviour. Because the images are drawn assuming the speed to be 1540 m/s, the bottom layer in Fig. 4b looks compressed because it takes less time for signals to arrive due to the faster speed. Later in Fig. 5, it is also demonstrated that the bottom layer with slower speeds looks expanded because it takes more time for signals to arrive. It is also noted that there is no reflection appearing on the medium boundary in the ultrasound image, because this is not included in our model.

After blurring, zero-mean white Gaussian noise is added to the simulated ultrasound image. The signal-to-noise ratio after the addition of the noise is 40 dB. The image is demodulated to baseband, envelope detected and logarithmically compressed into 60 dB dynamic range. In Fig. 4b, we can easily identify the artefacts typically associated with ultrasound imaging. The axial depth of the lateral focus corresponds to the designed centre of the middle circle. More serious blurring is easily spotted for scatterers away from the axial depth of the lateral focus. One can also notice the presence of coarser speckle in Fig. 4b due to the spatial averaging of the blur function.

3.3 Deconvolution via the correct sound speed

The blurred and noisy image in Fig. 4b is restored using the algorithm in [15, 16], whose core structure is briefly outlined in the appendix. It is noted that the deconvolution algorithm is identical to that used in the single-layered homogeneous medium. The only difference lies in the PSF used in the deconvolution.

An example result of the deconvolution is shown in Fig. 4c. The restored image proves that the true geometry of the reflectivity function can be recovered after the deconvolution via the same PSF which was used to make the corresponding ultrasound image in Fig. 4b. A high degree of restoration is observed. The circles appear again circular with sharp boundaries. Furthermore, the speckle size is significantly reduced and becomes comparably to that in the input data.

One may ask why the deconvolution result does not look perceptually the same as the designed reflectivity function despite the use of the same PSF for both forward and backward operations in the simulation. This is because of the presence of the additive Gaussian noise, and because of the blurring which involves loss of high frequency information and consequently causes the deblurring problem to be ill-posed.

3.4 Deconvolution via incorrect sound speeds

In Fig. 4c, we have shown the deconvolution result conducted with the correct sound speed for the bottom layer. In this subsection, we will see that deconvolution with an incorrect speed results in different characteristics to those in the single-layer case reported in [12]. These new features are found to be important in determining the speed in the dual-layer scenario.

Figure 5 shows the deconvolution based on PSFs with various bottom-layer speeds. The essence of the reflectivity function for the simulation is the same as that in Fig. 4a except the image size. The simulated ultrasound image in Fig. 5a was prepared to have the top-layer speed of 1540 m/s and that of the bottom layer 150 m/s slower. The rest of the images from Figs. 5b to 5f illustrate deconvolution results using PSFs with various bottom-layer speeds. The bottom-half images are observed in varying degrees of restoration. The speed of the top layer for these deconvolutions was maintained at the correct speed of 1540 m/s. Therefore, the top-half images are properly restored in all the deconvolutions.

It is clear that only the deconvolution with the correct speed in Fig. 5c can restore the geometry of the bottom layer properly. The deconvolutions (Figs. 5e and 5f) using bottom-layer speeds faster than that in the top-layer return the image with the bottom layer in varying degrees of axial expansion. This is because the deconvolution process is based on the assumption that the bottom-layer of the blurred ultrasound image in Fig. 5a has already gone through the compression indicated by the faster bottom-layer speed of its PSF. Subsequently the deconvolution tries to correct the effect by elongation, which ends up causing further expansion than the ultrasound image in Fig. 5a. In contrast, however, the deconvolutions (Figs. 5b and 5c) that use slower speeds return images with a bottom layer further shrunk.

It is also noted that the black strip towards the bottom of Fig. 5b is the result of an extreme compression through deconvolution. This is because the corresponding information is outside the image size used in the deconvolution. The consequence of this additional axial compression or expansion after deconvolution is that the numbers of horizontal image lines are different, e.g., for given circles in the bottom layers. This change may lead to a difficulty in picking up the correct speed in the bottom layer, because so-called like-for-like comparison is not possible. The phenomenon is explained in Sections 3.6 and 3.7.

3.5 Uncertainty in PSF parameters

In order to estimate the speed of sound accurately and reliably, the other parameters required to build a PSF must be correct as well. Our research group has recently studied the effects of uncertainty in the PSF on non-blind deconvolution [17]. The parameters of an ultrasound imaging PSF have been systematically investigated. It was shown that the speed of sound exhibited similar behaviour as the axial depth of a lateral focus for two-dimensional images. Therefore, the accuracy

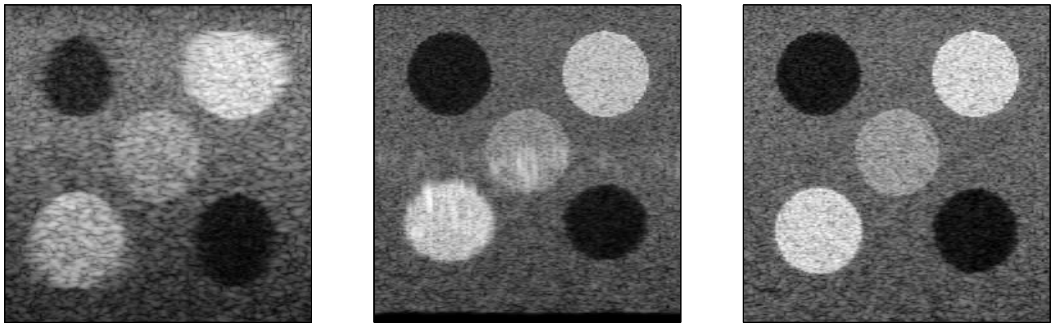

(a) Ultrasound image (b) $\Delta = -300$ m/s (c) $\Delta = -150$ m/s

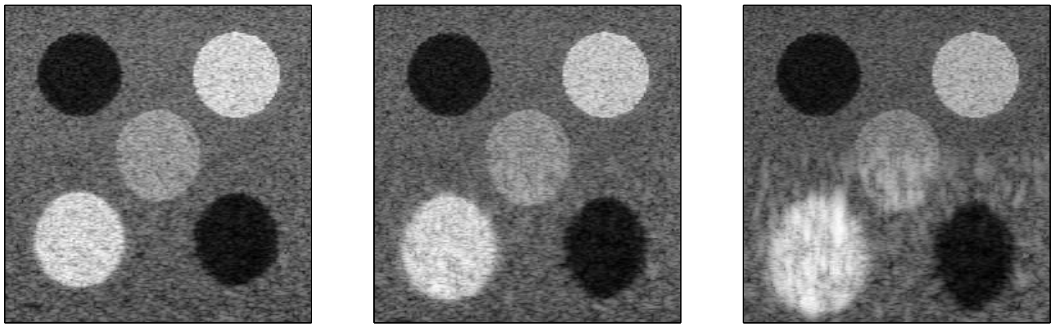

(d) $\Delta = 0$ m/s (e) $\Delta = +150$ m/s (f) $\Delta = +300$ m/s

Figure 5: Deconvolution images via various bottom-layer speeds with the layer boundary at the centre of the middle circle. (a) Simulated ultrasound image, in which the speed of the top layer is 1540 m/s, and that of the bottom layer 150 m/s slower. (b)∽(f) Deconvolution via PSFs with various bottom-layer speeds. The label at each image denotes the speed of the bottom layer, which is relative to 1540 m/s, while that of the top layer was kept 1540 m/s. These B-mode images were constructed assuming the sound speed of 1540 m/s.

of the sound-speed estimation may be affected by that of the lateral focus. In our speed-estimation framework, what matters for the lateral focus is not how the focus is realised through soft tissues, but the intended delay profile applied to the imaging system which is not disturbed by the tissue. Because we know the delay profiles that were used, it is unlikely that our estimation of the sound speed is susceptible to uncertainty in the lateral focus.

3.6 Correlation metric

The overall strategy of our speed estimation method is to run multiple deconvolutions using PSFs with different speeds and to pick the speed which produces the best restoration. Therefore, a metric capable of determining the best outcome is as crucial as the non-blind deconvolution algorithm itself. In our previous publication [12], we have successfully used the following metric to determine the sound speed of single-layered homogeneous media. Here, $\hat{\mathbf{x}}$ denotes the deconvolution image. The autocorrelation ($R_{\hat{\mathbf{x}}_i}[l]$) is calculated along the lateral line ($\hat{\mathbf{x}}_i$) at each i-th axial depth and then a summation ($\sum_l |R_{\hat{\mathbf{x}}_i}[l]|$) is made of the magnitude of all the l coefficients of the correlation. To produce a single-valued representation, another summation ($\sum_i \sum_l |R_{\hat{\mathbf{x}}_i}[l]|$) was taken of this value for all axial depths. For dual-layer situations in this paper, the correlation metric is restricted

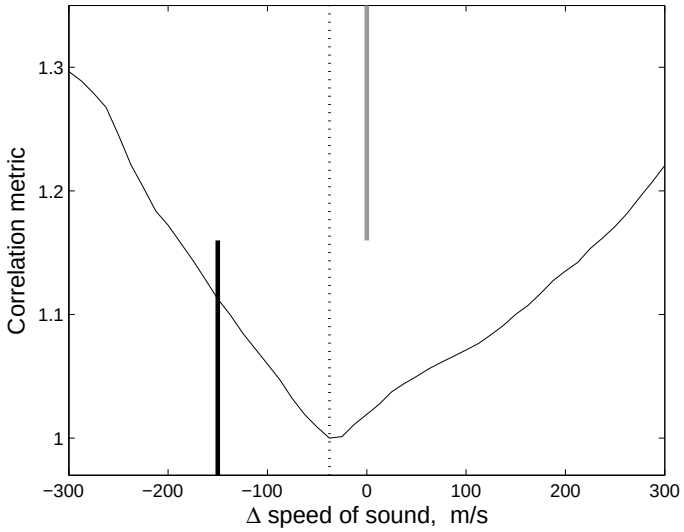

Figure 6: Plot of correlation metrics vs. various sound speeds in the bottom layer of a simulated dual-layered phantom. The correlation metric was applied to the bottom layer of the deconvolution images, and it is normalised by its minimum for display purposes. The reference speed ($\Delta = 0$) is 1540 m/s. The top-half grey vertical line denotes the speed of the top layer for reader's information, while the bottom-half black vertical line denotes the speed of the bottom layer which is being estimated. The dotted line with a full vertical length indicates the minimum of the correlation metric curve, which is the estimate of the bottom-layer speed. For vertical lines, the y-axis values are irrelevant. This convention will be applied to other similar graphs.

to the appropriate layer where the speed is estimated.

Figure 6 shows a graph of the aforementioned correlation metric for various bottom-layer speeds of sound in a simulated dual-layered phantom. Several B-mode images of this dataset have already been shown in Fig. 5. Because the sound speed of a bottom layer is being estimated in this figure, the correlation metric is applied to the bottom layer of deconvolution images. The behaviour of the correlation metric applied to the top layer is not shown throughout this article. Readers can find examples of this in our publication [12] that addresses the estimation of the sound speed in single-layered homogeneous media, since the methodology for top layers of dual-layered media is essentially identical to that for homogeneous media. The values of the correlation are normalised for display because the metric itself does not directly indicate a meaningful physical quantity but the relative differences are the most important. In this example, however, the graph indicates that the correlation metric has failed to identify the correct speed of sound for the bottom layer.

3.7 Interpolation of deconvolution images

In previous sections, we have described changes in the axial dimensions of bottom layers of deconvolution results and the failure of the correlation metric. Because the correlation metric was successfully used for single-layered homogeneous soft tissue [12] which does not incur the axial scale change, the cause of the failure is not likely to lie in the correlation metric itself, but perhaps in the extra change in the axial scale of deconvolution images. Such axial changes make the comparison of certain features, e.g. circles, inconsistent among deconvolutions, as they will have

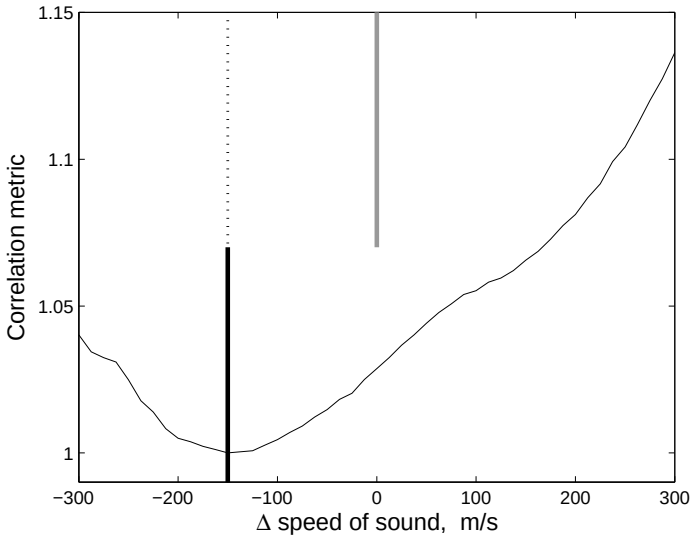

Figure 7: Plot of correlation metrics vs. various sound speeds in the bottom layer of a simulated dual-layered phantom. The deconvolution images were axially interpolated to make circles occupy the same number of horizontal image lines regardless of bottom-layer sound speeds in their PSFs.

different numbers of horizontal image lines inside them. Therefore, we have explored image interpolation strategies which make each feature intersect the same number of image lines regardless of the bottom-layer speed used in the PSFs.

One-dimensional linear interpolation is conducted along each A-line in the bottom layer. The interpolation ratio at each speed is determined by the inverse of its speed: a lower speed will have more interpolated horizontal lines than a higher speed, and hence the procedure subsequently makes the deconvolution images of lower speeds expand and those of higher speeds contract. Figure 7 illustrates a typical example of the correlation metric applied to interpolated deconvolution images. The original dataset is the same as that in Fig. 6. The correlation metric is now capable of detecting the correct speed of the bottom layer.

3.8 Cost of dual-layer PSFs

Each dual-layer PSF appearing in this article takes several hours to compute in Matlab environment. This expensive nature of dual-layer operation makes it difficult to implement an optimisation strategy to search for a minimum correlation, which was successfully adopted for a single-speed estimation [12]. Perhaps, the PSFs to produce the likes of Fig. 7 can be run concurrently by using multiple computing resources, but the PSFs for an optimisation process can only be calculated in series. Because we are only seeking to demonstrate the speed-estimation capability of our deconvolution algorithm in dual-layered medium, we have not pursued such an optimisation process, but analysed and displayed the correlation metric curves via numerous PSFs as illustrated in Fig. 7.

4 *In vitro* measurements

After verifying our sound-speed estimation technique in the simulated dual-layered media, we proceeded to apply the estimation algorithm to *in vitro* dual-layered datasets.

The following ultrasound system was used to acquire the RF data for *in vitro* measurements. The system consisted of a General Electric[¶] probe RSP6-12 and a Diasus ultrasound machine from Dynamic Imaging Ltd.[‖] which has 128 A-line capability and operates an active aperture of 32 piezoelectric elements, synchronised with a Gage[**] Compuscope CS14200 digitiser. The digitisation process was linked to the locally-developed Stradwin software[††], which is a user-friendly cross-platform tool for medical ultrasound acquisition and visualisation.

4.1 Preparation of in-house phantoms

We locally produced ultrasound tissue-equivalent phantoms by mixing agar powder, scatterers, propanol and water [21]. For dual-layered phantoms with each layer having different speed of sound, we created phantoms in two steps. First, a liquid form of phantom after heating and cooling of the aforementioned mixture is poured into an empty container, and was allowed to congeal. Several hours later, when the phantom has completely solidified, another liquid form of phantom with different composition was poured on top of the already solidified phantom. In this way, we prepared a pair of phantoms. One was made to have its top layer with thickness of 15.3 mm, and the other with 20.5 mm. The thickness of each top layer was evaluated later based on the estimated speeds of the top layer. The pair of phantoms were prepared such that the material in the top layer of one phantom is the same (and made together) as that in the bottom layer of the other phantom, and vice versa. For these in-house phantoms, the speed of sound in each layer is not known *a priori*. We measured their speeds by means of our deconvolution-based estimation method reported for a single-speed situation [12]: the speed measurement of the phantom material composing the top layer is a straightforward and direct implementation of the algorithm. Then, we treat the speed estimated for the top layer in one phantom as a gold standard for the speed to be estimated in the bottom layer of the other phantom through our dual-layer estimation algorithm.

4.2 Results of dual-layer algorithm applied to phantoms

Figures 8 and 9 illustrate examples of the correlation metric applied to these *in vitro* phantoms. For these datasets, the correlation metric is shown to detect the speeds of the bottom layer. The curve in Fig. 8 demonstrates the uneven nature of the metric and indicates a potential risk if a local-minimum based search method is applied. This local fluctuation may be related to the interpolation process. However it is found that a higher-order interpolation such as a cubic spline does not noticeably improve the situation. Currently, there is no clear indication of which RF dataset behaves better or worse after an axial interpolation is conducted. But, in general, correlation metrics with interpolation seem to detect the minimum with certain error bounds. More ultrasound acquisitions were carried out. For each phantom from the pair, a total of 8 measurements were conducted: 4 different lateral focus settings for 2 different locations in each

[¶] GE Healthcare, Pollards Wood, Nightingales Lane, Chalfont St Giles, BUCKS UK

[‖] Dynamic Imaging used to be based near Edinburgh in Scotland, but they are no longer in business.

[**] Gage Applied Technologies, 900 N. State Street, Lockport IL 60441, USA

[††] This is available free at http://mi.eng.cam.ac.uk/~rwp/stradwin/ .

phantom. The overall errors in the estimation of the bottom-layer speed were found to be:

-8.81 ± 15.62 m/s or -0.57 ± 1.01 % for the phantom in Fig. 8;

$+13.09 \pm 16.72$ m/s or $+0.87 \pm 1.12$ % for the phantom in Fig. 9.

Here the errors are presented in the notation of "mean ± standard deviation".

The results suggest that the errors of the dual-layer estimation method are not as good as those accomplished for our single-speed estimation. We reported -0.44 ± 0.31 % for a phantom made from an independent manufacturer and $+0.01 \pm 0.60$ % for locally made phantoms [12]. Note especially that the standard deviation in the single-speed method is much better than that of the dual-speed method. This may indicate that the dual-speed approach could be inherently less reliable than that of the single speed. To reach a workable model within the framework of our deconvolution method [15, 16], several assumptions have been made in earlier sections: for example, trivial reflection from a layer boundary parallel to the probe aperture, perfect plane wave incidence and refraction guided by Snell's law, and phantoms with pure fluid characteristics. In addition, there may be an error propagated from the estimation of the top-layer speed whose bounds were mentioned earlier in this paragraph.

Despite the reduced performance of our dual-layer estimation algorithm compared to our single-speed method, it is discovered that our dual-layer approach is still capable of producing an estimate better than or comparable to some other methods reported for local speed estimation. Kondo et al. [4] reported a standard deviation of 41.1 m/s when the mean speed was 1550 m/s. Their method was developed for estimating the speed of local regions which is more complicated than our dual-layer scenarios, but the quoted error was obtained from a single-speed homogeneous phantom consisting of agar and graphite particles. As a reminder, the standard deviation of our method for dual-layer phantoms is around 15 m/s. Using a transaxial compression technique, Ophir and Yazdi [5] measured the sound speed in the bottom layer of a dual-layered laboratory phantom made of polyester sponge, water and glycol solution. They reported a mean estimation error of +0.75 % for the bottom-layer speed of a single phantom, while the standard deviation of the error was not reported. Note that mean estimation errors for both of our *in vitro* phantoms are -0.57 and $+0.87$ %.

Figure 10 shows the ultrasound images for the phantom whose correlation metric for the bottom layer is shown in Fig. 9. The image (a) in Fig.10 is the original ultrasound image acquired by the aforementioned ultrasound system. The image (b) is the deconvolution via dual-layered PSF having estimated speeds of 1550 m/s and 1496.25 m/s for the top- and bottom-layer, respectively. In the images, one can see the bright horizontal lines which are indeed the boundary between the two layers of phantom materials. It is clear that the deconvolution image (b) is enhanced greatly from the original ultrasound image (a): the speckle size is reduced, and point-like scatterers especially further down the images are restored to be more distinct from their surroundings. One can also notice that the boundary line gets thinner as a result of deblurring in deconvolution, which may indicate that the amount of true reflection might not be as much as judged in the original image (a). An intriguing aspect about the boundary line is that it seems to be tilted after deconvolution, but this appears to be an optical illusion upon closer inspection.

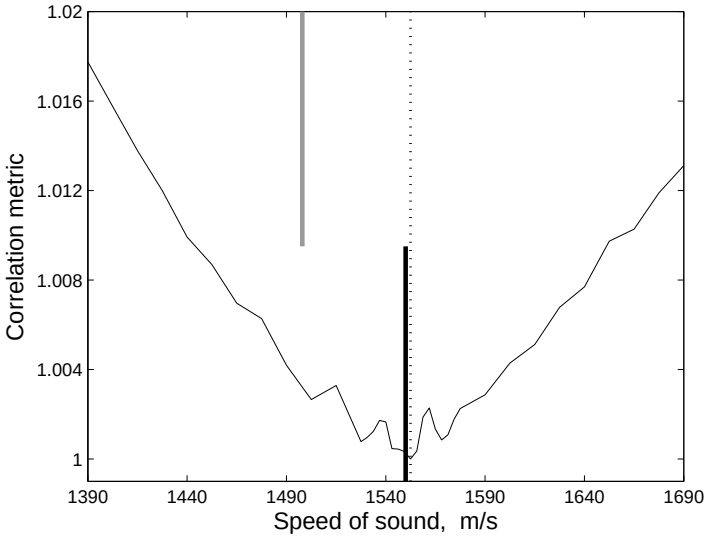

Figure 8: Plot of correlation metrics vs. various sound speeds in the bottom layer of an *in vitro* dual-layered phantom. The sound speeds are 1498 m/s in the top layer and 1550 m/s in the bottom layer, which are denoted by the top-half grey and the bottom-half black vertical lines, respectively. The error in the estimation of the bottom-layer speed is +2.5 m/s and is indicated by the full vertical-length dotted line.

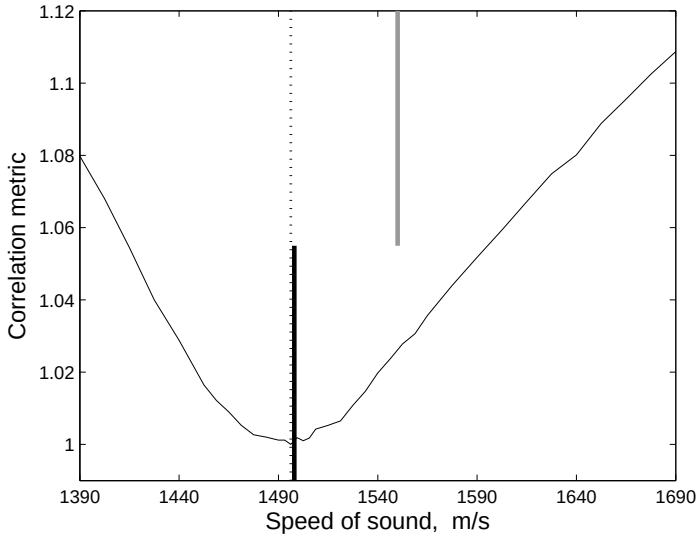

Figure 9: Plot of correlation metrics vs. various sound speeds in the bottom layer of an *in vitro* dual-layered phantom. The sound speeds are 1550 m/s in the top layer and 1498 m/s in the bottom layer, which are denoted by the top-half grey and the bottom-half black vertical lines, respectively. The error in the estimation of the bottom-layer speed is −1.75 m/s and is indicated by the full vertical-length dotted line.

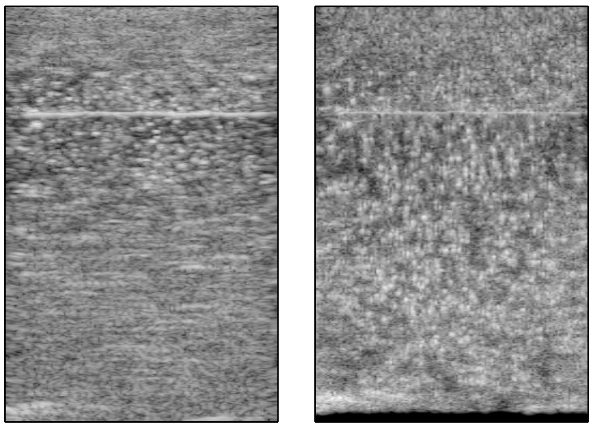

Figure 10: Ultrasound images of an *in vitro* in-house dual-layered phantom: (a) original ultrasound image, (b) deconvolution by dual-layered PSF with estimated speeds of 1550 m/s and 1496.25 m/s for the top- and bottom-layer, respectively. The size of the images is 38.1 mm $\times$ 25.0 mm, when the speed of sound is assumed to be 1540 m/s for comparison purposes. The ultrasound dataset is the same as that used in Fig. 9. The dynamic range of the logarithmically compressed images is 60 dB.

5 Conclusions

We have demonstrated that image deconvolution applicable to medical ultrasound systems can be used to estimate the speed of sound in dual-layered media. An ultrasound simulator has been developed specifically for dual-layered media. It is assumed that soft tissue can be treated as non-dispersive fluid, and it is found that pulse-echo ultrasound is mainly transmitted at the medium boundary for moderate speed differences. It is also shown that the refracted arrival times can be calculated using Snell's law. Unlike homogeneous media, it has been found that the deconvolution with dual-layered media requires axial interpolation for consistent comparison of correlation metrics among different speeds in the bottom layer.

Our estimation method for dual-layered media has been validated in simulations and *in vitro* phantoms. Its estimation errors were found to be -0.57 ± 1.01 % and $+0.87 \pm 1.12$ % (mean $\pm$ standard deviation) for a pair of *in vitro* in-house phantoms. Its uncertainty level is not as good as that of our estimation approach for homogeneous media, but is found to be better than or comparable to other local speed estimation methods where the data acquisition may not be as simple as in our proposed method.

6 Acknowledgements

The work was funded by the Engineering and Physical Sciences Research Council (reference EP/E007112/1) in the United Kingdom.

A Deconvolution Algorithm

The paper is mainly concerned with the estimation of the sound speed in pulse-echo ultrasound applications. But, the deconvolution of an ultrasound image is a pivotal part of our estimation process. Therefore, we briefly explain the key components of our deconvolution algorithm for the benefit of readers who may not be familiar with it. Complete details can be found in [15, 16].

A.1 Ultrasound image formation

The A-lines of an ultrasound imaging system can be mathematically modelled as a Fredholm integral of the first kind [15]. The wave propagation is assumed linear. Although non-linearity is present in *in vivo* scans of clinical applications, our approach is still applicable to most clinical ultrasound images which are usually dominated by linearity. In medical ultrasound imaging, linearity is generally preserved in pulse propagation and reflection, with higher order harmonic imaging as exceptions [22].

When we adopt a discrete space-time formulation, the integral can be further simplified using a vector-matrix notation with a complex random variable $\mathbf{x}$ as the reflectivity function and $\mathbf{y}$ as the complex analytic baseband counterpart of the measured ultrasound signal:

$$\mathbf{y} = \mathbf{H}\,\mathbf{x} + \mathbf{n}\;. \tag{5}$$

Potential measurement errors are taken into account as complex additive white Gaussian noise ($\mathbf{n}$). $\mathbf{H}$ is a block diagonal matrix along the lateral dimension. Each block matrix maps from the axial depth dimension to the time domain at a given lateral position. Here, two-dimensional data $(\mathbf{y}, \mathbf{x}, \mathbf{n})$ are rearranged into one-dimensional vector equivalents by lexicographic ordering, and thus the sizes of the vectors and the matrix are: $N \times 1$ for $\mathbf{x}$, $\mathbf{n}$, and $\mathbf{y}$, and $N \times N$ for $\mathbf{H}$. Here, N is the total dataset size.

A.2 Deconvolution under an Expectation-Maximisation (EM) framework

Our goal is to estimate a reflectivity function $\mathbf{x}$ from a noisy and blurred image $\mathbf{y}$. The algorithm operates in a Bayesian context. Because the finite resolution cell of a PSF merges the responses from neighbouring scatterers during the blurring process ($\mathbf{H}\,\mathbf{x}$), the deblurring procedure tends to be ill-posed, and therefore a direct inverse filtering is likely to fail. One of the standard solutions to this problem is to incorporate regularisation in a maximum *a posteriori* framework (MAP, see p.314 in [23]) with a prior on the reflectivity function:

$$\hat{\mathbf{x}} = \arg\,\max_{\mathbf{x}}\,\left[\ln\,p(\mathbf{y}\mid\mathbf{x},\sigma_n^2) + \ln\,p(\mathbf{x})\right]\;. \tag{6}$$

Here, $\hat{\mathbf{x}}$ is an estimate of the reflectivity function, obtained from the deconvolution process, and σ_n^2 the variance of $\mathbf{n}$. Possible priors could involve assuming Gaussian or Laplacian statistics for the reflectivity function. The Gaussian prior, in particular, leads to the well-known Wiener filter:

$$\hat{\mathbf{x}} = \arg\,\min_{\mathbf{x}}\,\left[\frac{1}{2\sigma_n^2}\|\mathbf{y}-\mathbf{H}\,\mathbf{x}\|^2 + \frac{1}{2}\mathbf{x}^H\mathbf{C}_x^{-1}\mathbf{x}\right] = (\mathbf{H}^H\mathbf{H} + \sigma_n^2\mathbf{C}_x^{-1})^{-1}\mathbf{H}^H\mathbf{y}\;. \tag{7}$$

In a further simplified case of $\mathbf{C}_x = \sigma_x^2 \mathbf{I}_N$, this is known as zero-order Tikhonov regularisation. The superscript H denotes the Hermitian transpose. The term $\mathbf{C}_x$ represents the covariance matrix $\mathbf{E}(\mathbf{x}\mathbf{x}^H)$ of $\mathbf{x}$, σ_x^2 the variance of $\mathbf{x}$, and $\mathbf{I}_N$ the identity matrix with size N. Instead of using this conventional prior for the entire tissue ($\mathbf{x}$), we model the tissue reflectivity as the product of microscopically randomised fluctuations ($\mathbf{w}$) and a macroscopically smooth tissue-type image called the echogenicity map ($\mathbf{S}$) which shares the characteristics of natural images [16]:

$$\mathbf{x} = \mathbf{S}\,\mathbf{w}\ . \tag{8}$$

Here, $\mathbf{w}$ is a $N \times 1$ complex vector, and $\mathbf{S}$ is a $N \times N$ diagonal matrix with real non-negative values. If a zero-mean Gaussian prior is assigned to $\mathbf{w}$, then $\mathbf{x}$ is also observed to be a zero-mean Gaussian when $\mathbf{S}$ is known. It leads to the conditional probability density function of $\mathbf{x}$, given $\mathbf{S}$:

$$p(\mathbf{x} \mid \mathbf{S}) \propto \frac{1}{|\mathbf{S}|^2} \exp\left(-\frac{1}{2}\mathbf{x}^H \mathbf{S}^{-2} \mathbf{x}\right)\ . \tag{9}$$

This implies two key procedures of our algorithm. First, when $\mathbf{S}$ is known, then $\mathbf{x}$ can be found using the Wiener filter in Eq. (7) with $\mathbf{S}^2$ representing the covariance matrix. Second, when $\mathbf{x}$ is known from the first step and $\ln|w_i|$ is treated as additive noise, then $\mathbf{S}$ can be determined through a denoising process:

$$\ln S_i = \ln|x_i| - \ln|w_i|\,, \qquad i = 1, \cdots, N\ . \tag{10}$$

The subscript i denotes the element of the vectors and the diagonal matrix, and $|\cdot|$ the modulus of a complex variable. Using an Expectation-Maximisation (see p.285 in [23]) framework, we can construct an iterative deconvolution strategy alternating between the Wiener filter for $\mathbf{x}$ (Expectation step) and the denoising for $\mathbf{S}$ (Maximisation step).

For denoising, we adopted a wavelet-based algorithm to separate $\mathbf{x}$ into its $\mathbf{S}$ and $\mathbf{w}$ components. We therefore represent the reflectivity function ($\mathbf{x}$) using the dual-tree complex wavelet transform DT-$\mathbb{C}$WT [24, 25] which has been shown to be particularly effective in denoising applications [26].

References

[1] M. E. Anderson, M. S. McKeag, and G. E. Trahey, "The impact of sound speed errors on medical ultrasound imaging", Journal of the Acoustical Society of America **107**, 3540–3548 (2000).

[2] N. Hayashi, N. Tamaki, M. Senda, K. Yamamoto, Y. Yonekura, K. Torizuka, T. Ogawa, K. Katakuraand, C. Umemura, and M. Kodama, "A new method of measuring in vivo sound speed in the reflection mode", Journal of Clinical Ultrasound **16**, 87–93 (1988).

[3] D. E. Robinson, J. Ophir, L. S. Wilson, and C. F. Chen, "Pulse-echo ultrasound speed measurements: progress and prospects", Ultrasound in Medicine & Biology **17**, 633–646 (1991).

[4] M. Kondo, K. Takamizawa, M. Hirama, K. Okazaki, K. Iinuma, and Y. Takehara, "An evaluation of an in vivo local sound speed estimation technique by the crossed beam method", Ultrasound in Medicine & Biology **16**, 65–72 (1990).

[5] J. Ophir and Y. Yazdi, "A transaxial compression technique (TACT) for localized pulse-echo estimation of sound speed in biological tissues", Ultrasonic Imaging **12**, 35–46 (1990).

[6] Y. Saijo, E. S. Filho, H. Sasaki, T. Yambe, M. Tanaka, N. Hozumi, K. Kobayashi, and N. Okada, "Ultrasonic tissue characterization of atherosclerosis by a speed-of-sound microscanning system", IEEE Transactions on Ultrasonics, Ferroelectrics, and Frequency Control **54**, 1571–1577 (2007).

[7] T. L. Chenevert, D. I. Bylski, P. L. Carson, C. R. Meyer, P. H. Bland, D. D. Adler, and R. M. Schmitt, "Ultrasonic computed tomography of the breast", Radiology **152**, 155–159 (1984).

[8] M. P. André, H. S. Janée, P. J. Martin, G. P. Otto, B. A. Spivey, and D. A. Palmer, "High-speed data acquisition in a diffraction tomography system employing large-scale toroidal arrays", International Journal of Imaging Systems and Technology **8**, 137–147 (1997).

[9] N. Duric, P. Littrup, O. Rama, and E. Holsapple, "Computerized ultrasound risk evaluation (CURE): first clinical results", in *Acoustical Imaging*, edited by M. P. André, 173–181, the 28th International Symposium on Acoustical Imaging (Springer) (2005).

[10] J. Wiskin, D. T. Borup, S. A. Johnson, M. Berggren, T. Abbott, and R. Hanover, "Full-wave, non-linear, inverse scattering: high resolution quantitative breast tissue tomography", in *Acoustical Imaging*, edited by M. P. André, 183–193, the 28th International Symposium on Acoustical Imaging (Springer) (2005).

[11] M. P. André, C. H. Barker, N. Sekhon, J. Wiskin, D. Borup, and K. Callahan, "Pre-clinical experience with full-wave inverse-scattering for breast imaging: Sound speed sensitivity", in *Acoustical Imaging*, edited by I. Akiyama, 73–80, the 29th International Symposium on Acoustical Imaging (Springer, Shonan, Japan) (2007).

[12] H.-C. Shin, R. Prager, H. Gomersall, N. Kingsbury, G. Treece, and A. Gee, "Estimation of speed of sound using medical ultrasound image deconvolution", Technical Report CUED/F-INFENG/TR626, Cambridge University Engineering Department (2009), available on-line: http://mi.eng.cam.ac.uk/reports/index-biomed.html.

[13] D. Napolitano, C.-H. Chou, G. McLaughlin, T.-L. Ji, L. Mo, D. DeBusschere, and R. Steins, "Sound speed correction in ultrasound imaging", Ultrasonics **44**, e43–e46 (2006).

[14] K. Richter and S. H. Heywang-Köbrunner, "Sonographic differentiation of benign from malignant breast lesions: Value of indirect measurement of ultrasound velocity", American Journal of Roentgenology **165**, 825–831 (1995).

[15] J. Ng, R. Prager, N. Kingsbury, G. Treece, and A. Gee, "Modeling ultrasound imaging as a linear shift-variant system", IEEE Transactions on Ultrasonics, Ferroelectrics, and Frequency Control **53**, 549–563 (2006).

[16] J. Ng, R. Prager, N. Kingsbury, G. Treece, and A. Gee, "Wavelet restoration of medical pulse-echo ultrasound images in an EM framework", IEEE Transactions on Ultrasonics, Ferroelectrics, and Frequency Control **54**, 550–568 (2007).

[17] H.-C. Shin, R. Prager, J. Ng, H. Gomersall, N. Kingsbury, G. Treece, and A. Gee, "Sensitivity to point-spread function parameters in medical ultrasound image deconvolution", Ultrasonics **49**, 344–357 (2009).

[18] L. E. Kinsler, A. R. Frey, A. B. Coppens, and J. V. Sanders, *Fundamentals of Acoustics*, 3rd edition (John Wiley & Sons, New York) (1982).

[19] B. A. J. Angelsen, *Ultrasound Imaging: Waves, Signals, and Signal Processing*, volume I (Emantec AS, Trondheim, Norway) (2000).

[20] J. Jensen and N. B. Svendsen, "Calculation of pressure fields from arbitrarily shaped, apodized, and excited ultrasound transducers", IEEE Transactions on Ultrasonics, Ferroelectrics, and Frequency Control **39**, 262–267 (1992).

[21] M. M. Burlew, E. L. Madsen, J. A. Zagzebski, R. A. Banjavic, and S. W. Sum, "A new ultrasound tissue-equivalent material", Radiation Physics **134**, 517–520 (1980).

[22] T. Taxt, "Three-dimensional blind deconvolution of ultrasound images", IEEE Transactions on Ultrasonics, Ferroelectrics, and Frequency Control **48**, 867–871 (2001).

[23] C. W. Therrien, *Discrete Random Signals and Statistical Signal Processing* (Prentice Hall, Inc, Englewood Cliffs, NJ, USA) (1992).

[24] N. Kingsbury, "Image processing with complex wavelets", Philosophical Transactions of The Royal Society of London Series A **357**, 2543–2560 (1999).

[25] N. Kingsbury, "Complex wavelets for shift invariant analysis and filtering of signals", Applied and Computational Harmonic Analysis **10**, 234–253 (2001).

[26] L. Sendur and I. W. Selesnick, "Bivariate shrinkage functions for wavelet-based denoising exploiting interscale dependency", IEEE Transactions on Signal Processing **50**, 2744–2756 (2002).